



CHORUS

This is the accepted manuscript made available via CHORUS. The article has been published as:

Separating electrons and holes by monolayer increments in van der Waals heterostructures

Frank Ceballos, Peymon Zereshki, and Hui Zhao

Phys. Rev. Materials **1**, 044001 — Published 6 September 2017

DOI: [10.1103/PhysRevMaterials.1.044001](https://doi.org/10.1103/PhysRevMaterials.1.044001)

Separating Electrons and Holes by Monolayer Increments in van der Waals Heterostructures

Frank Ceballos, Peymon Zereshki, and Hui Zhao*

*Department of Physics and Astronomy, The University of Kansas,
Lawrence, Kansas 66045, United States*

(Dated: July 12, 2017)

Abstract

Since the discovery of graphene and its outstanding chemical, optical, and mechanical properties, other layered materials have been fiercely hunted for throughout various techniques. Thanks to their van der Waals interaction, acting as weak glue, different types of layered materials with mismatched lattices can be stacked with high quality interfaces. The properties of the resulting multilayer structures can be tune by choice of the materials, layer thicknesses, and sequence in which they are arranged. This opens the possibility for a large array of applications across many different fields. Here we present a systematic study with two-dimensional stacked layered materials, where their properties are tailored monolayer by monolayer. By arranging WSe_2 , MoSe_2 , WS_2 , and MoS_2 monolayers in predetermined sequences, that are predicted to have a ladder band alignment in both the conduction and valence bands, we separate electrons and holes between the two utmost layers by monolayer increments. The samples studied are a WSe_2 monolayer, a WSe_2 - MoSe_2 bilayer, a WSe_2 - MoSe_2 - WS_2 trilayer, and a WSe_2 - MoSe_2 - WS_2 - MoS_2 four-layer. We observe an increase in absorbance, a decrease in photoluminescence, a variation in interlayer charge transfer, and photocarrier lifetimes that are extended up to a few nanoseconds as additional layers were added. With these results, we demonstrate that van der Waals stacked two-dimensional materials can form effective complex stacks and are promising platforms for fabricating ultrathin and flexible optoelectronics.

I. INTRODUCTION

For several decades, the thickness of materials has been used to tailor their properties. Modern molecular-beam epitaxy technique allows fabrication of atomically thin films on lattice-matching substrates. The confinement of electrons in such quantum-well structures allows the tuning of their electronic and optical properties¹⁻³. The newly developed two-dimensional (2D) materials based on layered crystals provide unprecedented control of thickness down to sub-nanometers⁴⁻⁸. It was discovered that at such a scale the electronic and optical properties of materials change dramatically with thickness. For example, monolayer (1L)^{9,10}, bilayer (2L)¹¹⁻¹³, and trilayer (3L)¹⁴ graphene all show distinct charge transport properties¹⁵. In transition metal dichalcogenides (TMDs), such as MoS₂ and WS₂, the indirect bandgap increases significantly as the thickness approaches few-layer limit, making them direct-gap semiconductors at 1L^{16,17}. Stimulated by these discoveries, significant effort has been devoted to identifying, fabricating, and characterizing various 1L materials. Once the ultimate limit of the thickness has been achieved, the 1Ls are used to fabricate multilayer heterostructures - the so-called van der Waals heterostructures^{18,19}. Since 1Ls with different properties can be combined with little restrictions and with nearly perfect interface qualities, this approach provides a new route for material discovery.

So far, most studies of van der Waals heterostructures have focused on combining two 1Ls²⁰⁻²⁵, which laid the foundation for developing multilayer structures combining several 1Ls. Here we report a comprehensive study on the evolution of the optical properties of multilayer TMD as 1L components are introduced one by one. Starting with a WSe₂ 1L, we found systematic variation of the absorption, photoluminescence (PL), interlayer charge transfer, and photocarrier lifetime as new 1Ls are added to it, with the order of MoSe₂, WS₂, and MoS₂. This sequence forms a ladder alignment in both the conduction and the valence bands, with electrons and holes residing in the two utmost layers. We show that the resulting TMD 4L of WSe₂-MoSe₂-WS₂-MoS₂ possesses an enhanced peak absorbance of about 50%, corresponding to an absorption coefficient on the order of 10⁶ cm⁻¹. The photocarrier lifetime is extended up to several nanoseconds. These results show that such TMD multilayers can be used for ultrathin, flexible, and highly efficient photovoltaic and photodetection devices.

II. EXPERIMENTAL PROCEDURES

A. Sample Preparation

The WSe₂, MoSe₂, WS₂, and MoS₂ flakes were first mechanically exfoliated from bulk crystals using adhesive tape. A fraction of the numerous flakes on the tape were then transferred onto clear and flexible polydimethylsiloxane (PDMS) substrates by slightly pressing the tape onto a substrate and quickly peeling it off. The PDMS substrates were inspected under an optical microscope and 1Ls were identified by their optical contrast and later confirmed by PL spectroscopy. Depending on the type of measurements being conducted on the samples, the 1Ls were then transferred onto a quartz substrate or a silicon wafer capped with 90-nm of silicon dioxide, utilizing a micro-manipulator. The samples were then thermally annealed at 200°C for 2 hours under a H₂/Ar (20 sccm / 100 sccm) environment at a base pressure of about 2 - 3 Torr. For multilayer structures, after the annealing process, a different 1L was transferred precisely on top of the flake already placed on the substrate. The new sample was again annealed under the same conditions mentioned above. This procedure was repeated until a sample with desired number of layers was obtained.

The samples were kept under the ambient condition at 300 K for all the measurements.

B. Absorption Spectroscopy

Reflection contrast measurements were performed with a broadband tungsten-halogen light source, which output was spatially filtered with a pinhole and a pair of lens. Upon normal incidence, the light was focused to a spot size of about 2 - 3 μm by an objective lens. The incident power was about 0.05 μW for all the measurements. The reflected light from the sample was then collimated with the same objective lens and directed to a spectrometer equipped with a thermoelectrically cooled charge-coupled-device camera. For a sufficiently thin sample on a transparent and thick substrate (in this case, quartz), the absorbance of the samples can be calculated from the fractional change of reflectance by the sample, which is defined as $(R_{S+Q} - R_Q) / R_Q$, where R_{S+Q} and R_Q are, respectively, the reflectance of the sample (on quartz) and the reflectance of the quartz substrate. The absorbance can be obtained by $A = (1/4)(n^2 - 1)(R_{S+Q} - R_Q) / R_Q$, where n denotes the index of refraction of quartz²⁶.

C. Photoluminescence Spectroscopy

The PL spectroscopy measurements were carried using a 405-nm continuous-wave laser at normal incident with respect to the samples. The power of the laser was about $0.5 \mu\text{W}$. It was focused with a microscope objective lens to a spot size of about $1.0 \mu\text{m}$. The PL from the sample was collected by the same objective lens and directed into the spectrometer. To prevent the unwanted light from reaching the detector and affecting the PL measurement, a set of filters was placed before the spectrometer.

D. Transient Absorption Measurements

In the transient absorption setup, a 532-nm and 10-W diode laser was used to pump a Ti-sapphire laser, which generates 100-fs pulses with a repetition rate of 80 MHz and an average power of 2 W. For some measurements, the Ti-sapphire laser was tuned to 750 or 790 nm, depending on the sample being measured. Part of this beam (about 20%) was sent into a photonic-crystal fiber for supercontinuum generation, which outputs a broadband pulse. A band-pass filter with a 10-nm bandwidth was used to select the desired wavelength for the measurement. These two beams were used as pump and probe for the measurements. Since the photonic-crystal fiber is inefficient in generating light at wavelengths shorter than 500 nm, for measurements requiring such wavelengths as the pump, the Ti-sapphire output was tuned to 800 nm and sent into a beta barium borate (BBO) crystal to generate its second harmonic at 400 nm. The probe was then obtained from the photonic-crystal fiber.

In each pump-probe configuration, both the pump and the probe beams were linearly polarized along perpendicular directions, aligned along the same optical path using beamsplitters, and focused on the sample with a microscope objective lens to spot sizes of $1.5 - 2.5 \mu\text{m}$ in full-width at half-maximum. The reflected beams were then collected and collimated by the same objective lens and directed into a biased silicon photodiode. To prevent the reflected pump from reaching the photodiode, a set of filters was placed before the detector. The output of the photodiode is measured by a lock-in amplifier, which is synchronized with a mechanical chopper that modulates the pump intensity at about 2 KHz. With this setup, we can measure the differential reflection, which is defined as the normalized change of the probe reflectivity induced by the pump, $\Delta R/R_0 = (R - R_0)/R_0$, where R and R_0 are the reflectivities of the probe with and without the

presence of the pump beam, respectively. The differential reflection was measured as a function of probe delay, which is defined as the arrival time of the probe pulse at the sample with respect to the pump pulse.

III. RESULTS AND DISCUSSION

A. Optical Properties and Photocarrier Dynamics of the Monolayers

To better understand the evolution of properties with the number of layers, we begin by characterizing the relevant properties of the four component 1Ls used to fabricate the multilayers. The first row of Fig. 1 shows the microscope images of the 1L samples, with the 1L regions marked by the lines. The absorbance spectra of these 1L samples are shown in the second row, with A- and B-exciton resonances labeled. These spectra are consistent with previously reported results^{27,28}. The third row of Fig. 1 shows PL spectra of the 1Ls, with main peaks at the A-exciton resonances. The significantly higher PL yield observed, compared to the multilayer regions on the same flakes, further confirms their 1L thickness.

To probe the photocarrier lifetimes of 1Ls, time-resolved differential reflection measurements were performed. For each 1L, photocarriers were injected by a pump pulse tuned above the optical band gap and detected by a probe pulse tuned to the A-exciton resonance. The results are shown in the last row of Fig. 1. The peak differential reflection signal is confirmed to be proportional to the pump fluence, and thus proportional to the injected carrier density. Therefore, the decay of the signal reflects the loss of photocarrier population due to recombination. By exponential fits, shown as the solid lines, the photocarrier lifetimes are deduced, which are indicated in the figure. Previously, photocarrier lifetime in 1L TMDs have been studied by transient absorption^{29–35}, time-resolved PL^{36–41}, and transient THz techniques³⁸. A relatively large range of values have been obtained in these studies, which indicates that the lifetimes are sensitive to the sample quality, and is hence mainly limited by nonradiative recombination of carriers due to defects⁴². Our results are in line with these reports. We note that in these fits, an adjustable constant is included, which is at most a few percent of the peak, but much larger than the signal at negative probe delays. Since the separation of two sequential pump pulses is about 13 ns, the absence of a noticeable signal at negative probe delays indicates that the effects causing this slow-decaying component only persist for at most a few ns. Such a long-lived feature could be attributed to thermal effects

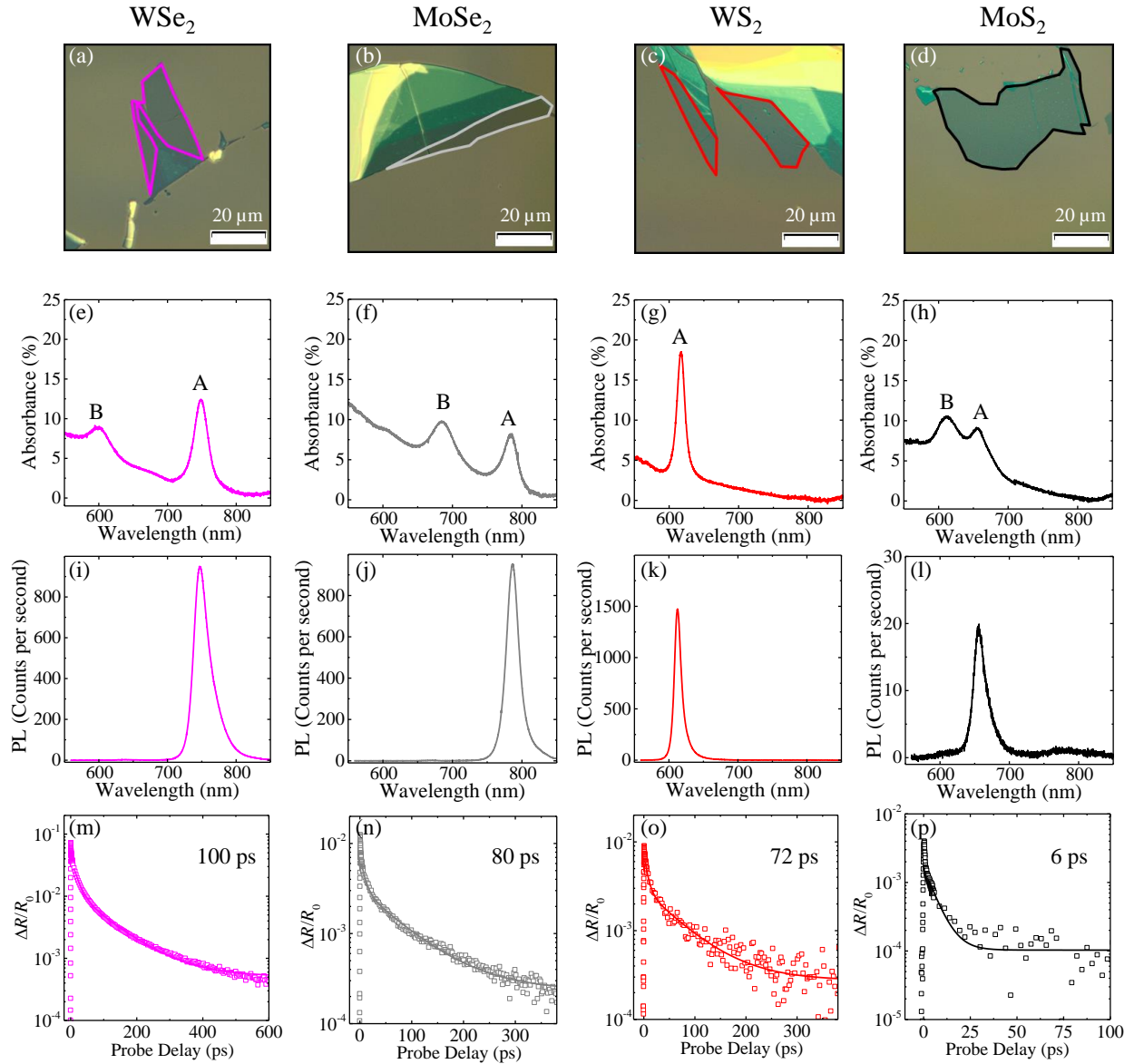


FIG. 1. Optical microscope images (first row), absorbance spectra (second row), photoluminescence spectra (third row), and differential reflection (last row) of the monolayers of (from left to right) WSe₂, MoSe₂, WS₂, and MoS₂. Numbers in the last row are photocarrier lifetimes deduced from exponential fits (solid curves).

or trapped carriers. Nevertheless, this nonzero background does not influence deduction of the carrier lifetime.

B. Optical Properties of Heterostructure Multilayers

We next discuss the change of the optical properties of multilayer samples as 1Ls are introduced. The samples include a WSe_2 1L, a WSe_2 - MoSe_2 2L, a WSe_2 - MoSe_2 - WS_2 3L, and a WSe_2 - MoSe_2 - WS_2 - MoS_2 4L, as shown in the first row of Fig. 2. This layer sequence is chosen so that the electrons and holes excited have the largest separation. According to first-principle calculations, these multilayers form ladder band alignment^{43,44}. As schematically shown in the second row of Fig. 2, the valence band maximum (VBM) is located in the bottom WSe_2 layer while the conduction band minimum (CBM) is in the top layer in all these samples. Consequently, electrons and holes (blue and yellow circles, respectively) are inclined to separate between the layers in order to populate the lowest energy states available. Purposely the arrangement of the layers in the multilayer samples is designed to maximize the separation between the electron and holes.

The evolution of the absorbance spectrum as new 1Ls were introduced is illustrated in the third row of Fig. 2. Panel (i) shows the absorbance of WSe_2 1L, which is replotted from Fig. 1(e). The absorbance reaches 12% at 749 nm, the A-exciton resonance of WSe_2 . The absorbance spectrum of the WSe_2 - MoSe_2 2L, shown as the blue curve in Fig. 2(j), closely resembles the sum of the individual spectra (orange curve) that was obtained by adding the spectra of the composing 1Ls. Noticeable differences start to be visible when comparing the spectrum from WSe_2 - MoSe_2 - WS_2 3L [blue curve in (k)] and that put together by summing the composing 1L spectra (orange curve). The 3L sample absorbs approximately 1 - 1.5 times more light over the wavelength range studied with the two evident peaks from WSe_2 and WS_2 red shifted by 10 - 15 nm. The shift can be attributed to the different dielectric environment present in different samples⁴⁵. Following a similar trend, in the WSe_2 - MoSe_2 - WS_2 - MoS_2 4L, the absorbance, blue curve in panel (l), is increased by a factor of 1.5 - 2 when compared to the sum of the four individual 1L absorbance spectra, orange curve in (l).

The enhanced absorption in multilayers could be attributed to the broadening of the exciton resonances due to the reduced lifetime of excitons in these 1Ls⁴⁶, which is a consequence of ultrafast charge transfer between these layers^{22,47}. Since the samples are multilayers on a substrate, interference between the reflected fields from the sample surface and from all the interfaces can affect the absorbance. To probe this effect, we used Rouard's method⁴⁸ to calculate reflection and transmission coefficients, respectively, for a system of several thin films on a thick and transparent

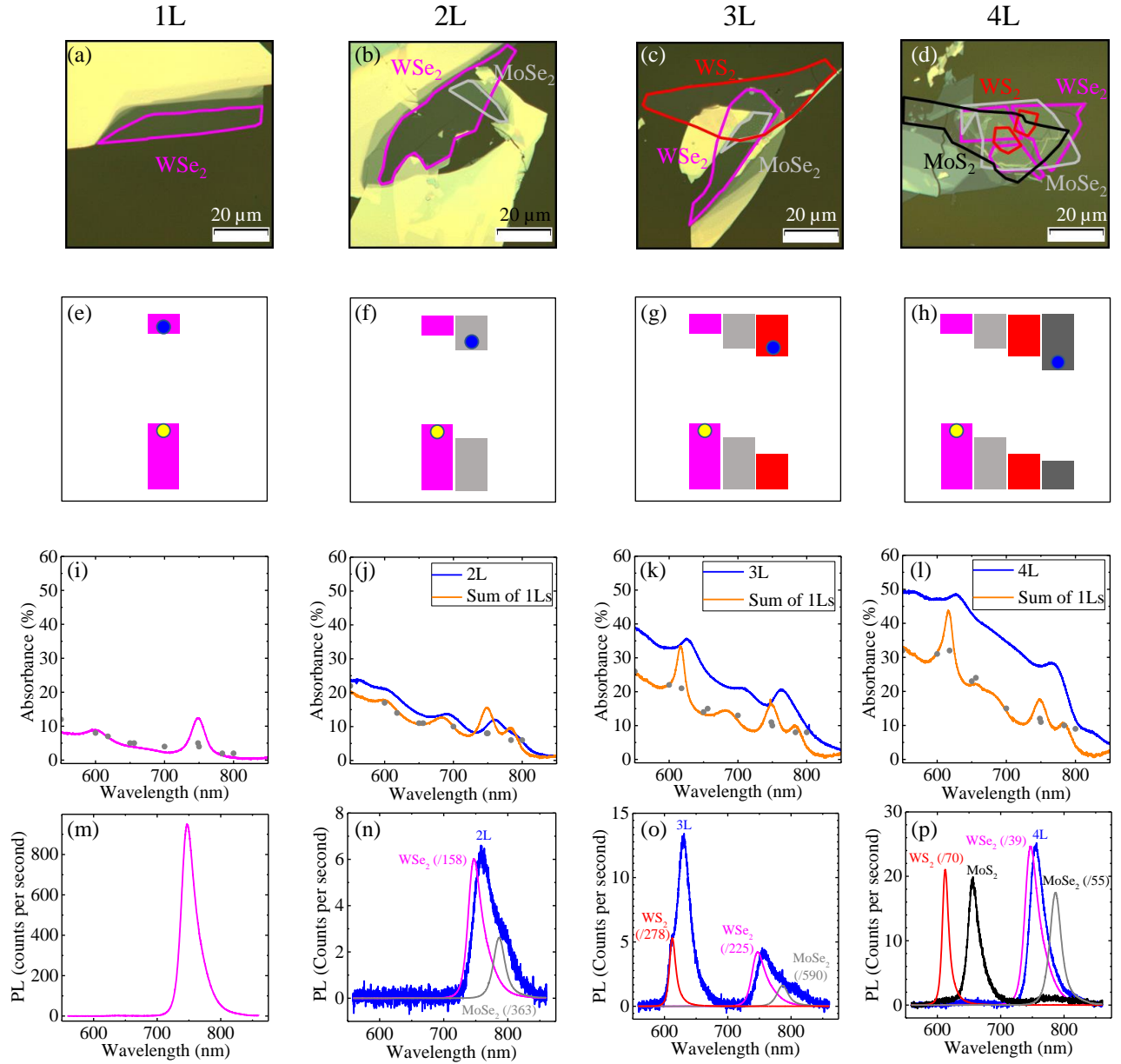


FIG. 2. Optical microscope images (first row), expected alignment of conduction (upper boxes) and valence bands (lower boxes, second row), absorbance spectra (third row), and photoluminescence spectra (last row) of WSe₂ 1L (first column), WSe₂-MoSe₂ 2L (second column), WSe₂-MoSe₂-WS₂ 3L (third column), and WSe₂-MoSe₂-WS₂-MoS₂ 4L (fourth column). In the absorbance spectra, the orange curve and gray symbols are calculated from the 1L spectra without and with interference effect included, respectively. The pink and blue curves are measured results.

substrate. This method accounts for the reflected photons at each interface and those absorbed within each layer. The calculation was performed for several selected wavelengths, using the complex indices of refraction of each layer reported in Ref. 27. The results are plotted as the gray symbols in Fig. 2(i)-(l). The agreement between these values and those obtained without considering the interference effect (orange curves) confirms the insignificant role of the interference effect in this situation. The discrepancy around the exciton peaks could be attributed to the possible differences in the characteristics of the exciton peaks between the CVD samples used in Ref. 27 and our exfoliated samples. Although more efforts are needed to fully understand the mechanisms of the absorption enhancement, it is encouraging that the peak absorbance of the 4L sample, with a thickness of only 2.5 nm, is about 50%. This corresponds to an absorption coefficient of about two to three orders of magnitude higher than in conventional bulk semiconductors.

The high absorbance of such van der Waals hetero-multilayers suggests their potential uses in ultrathin and flexible photovoltaic and photodetection devices as a light-absorbing layer. For such applications, the properties of photocarriers, especially their lifetime, are also important. To understand the photocarrier dynamics in these samples, we first use PL spectroscopy to probe the effectiveness of the interlayer charge transfer. Figure 2(m) shows the PL spectrum of WSe₂ 1L [replotted from Fig. 1(i)], which displays a pronounced peak at 749 nm. We then measured the PL spectrum from the WSe₂-MoSe₂ 2L, shown as the blue curve in (n). The PL spectra from WSe₂ and MoSe₂ 1Ls are shown, with their representative colors, with the quenching factors labeled in the legend. The strong quenching of the PL from the 2L structure is a clear indicator of effective charge transfer^{24,45,49-54}; that is, the interlayer charge transfer occurs on a time scale much shorter than the lifetime of excitons. Significant quenching of PL is only achievable in samples with high quality interfaces, which are formed after the annealing procedure. Before annealing, the PL of the 2L sample simply mimics the sum of the two 1L PL spectra. We note that no PL peaks from the spatially indirect (interlayer) excitons formed after charge transfer were observed in our experiment. Recently, strong PL of indirect excitons in WSe₂-MoSe₂ heterostructures has been observed at low temperatures^{25,49,55}. However, at room temperature, it was expected to be at about 900 nm, which is out of the detection range of our experiment. It is also expected to be much weaker than the WSe₂ exciton peak, since even at 200 K it is only a fraction of the WSe₂ peak⁵⁵.

The PL spectrum from the WSe₂-MoSe₂-WS₂ 3L, the blue curve in (o), displays several spectral features. First, the WSe₂, MoSe₂, and WS₂ PL peaks are quenched by factors of 225, 590, and 278, respectively. Secondly, a pronounced fourth peak at 630 nm is observed, which has been previously

identified as the radiative recombination of trions in a MoSe₂-WS₂ sample⁵³. The indirect excitons in the 3L structure is expected to radiate at a longer wavelength than 2L (due to the ladder band alignment) and with a lower yield (due to the larger separation of electrons and holes). Hence, it was not observed in our experiment. Finally, the 4L PL spectrum, blue curve in (p), shows one distinctive quenched peak corresponding to the WSe₂ 1L. Interestingly, we note that the WSe₂ peak in the 4L is about 6 times stronger than in the 3L. The origin of this counter-intuitive observation will be discussed after the results of time-resolved measurements are presented.

C. Electron Transfer and Lifetime

Having confirmed that the samples form effective heterojunctions between adjacent layers, we proceed to time-resolve the dynamics of the photocarriers in the multilayer samples with the pump-probe configurations shown in the first row of Fig. 3. Here, a linearly polarized pump pulse (blue arrows) is used to inject photocarriers which are then monitored by measuring the differential reflection, $\Delta R/R_0$, of a time delayed probe pulse (green arrows) tuned to the A-exciton resonance of a given layer. For each sample, measurements were performed with different values of pump fluence, and hence different injected carrier densities. We found that the signal magnitude is approximately proportional to the injected carrier density, and the temporal behavior is independent of the density. Figure 3 shows results where the total injected carrier density is $1.5 \times 10^{11} \text{ cm}^{-2}$. This value was estimated from pump fluence by using Rouard's method discussed above.

The first column of Fig. 3 shows the differential reflection signal from the WSe₂ 1L sample for short (e) and long time ranges (i). The pump and probe wavelengths are 400 and 749 nm, respectively. The signal reaches to the peak at an ultrashort time scale. The orange curve in (e) is the integral of a Gaussian function with a full-width at half-maximum of 0.35 ps, obtained from the intensity cross-correlation of the pump and probe pulses. Since the time evolution of the differential reflection signals are exponential, it is desirable to correlate such a temporal width to the time constant of exponentially varying functions. For this purpose, we fit the orange curve with a function, $\Delta R/R_0(t) = A_0[1 - \exp(-t/\tau)]$. The black dashed line indicates the best fit with a time constant of $\tau = 0.18 \text{ ps}$. This exercise shows that the instrument is capable of measuring exponentially varying functions with a time resolution of 0.18 ps. The fact that the differential reflection signal closely follows the response curve indicates that the actual rising time of the signal is significantly shorter than 0.18 ps. The decay of the signal (i) can be fit by an exponential

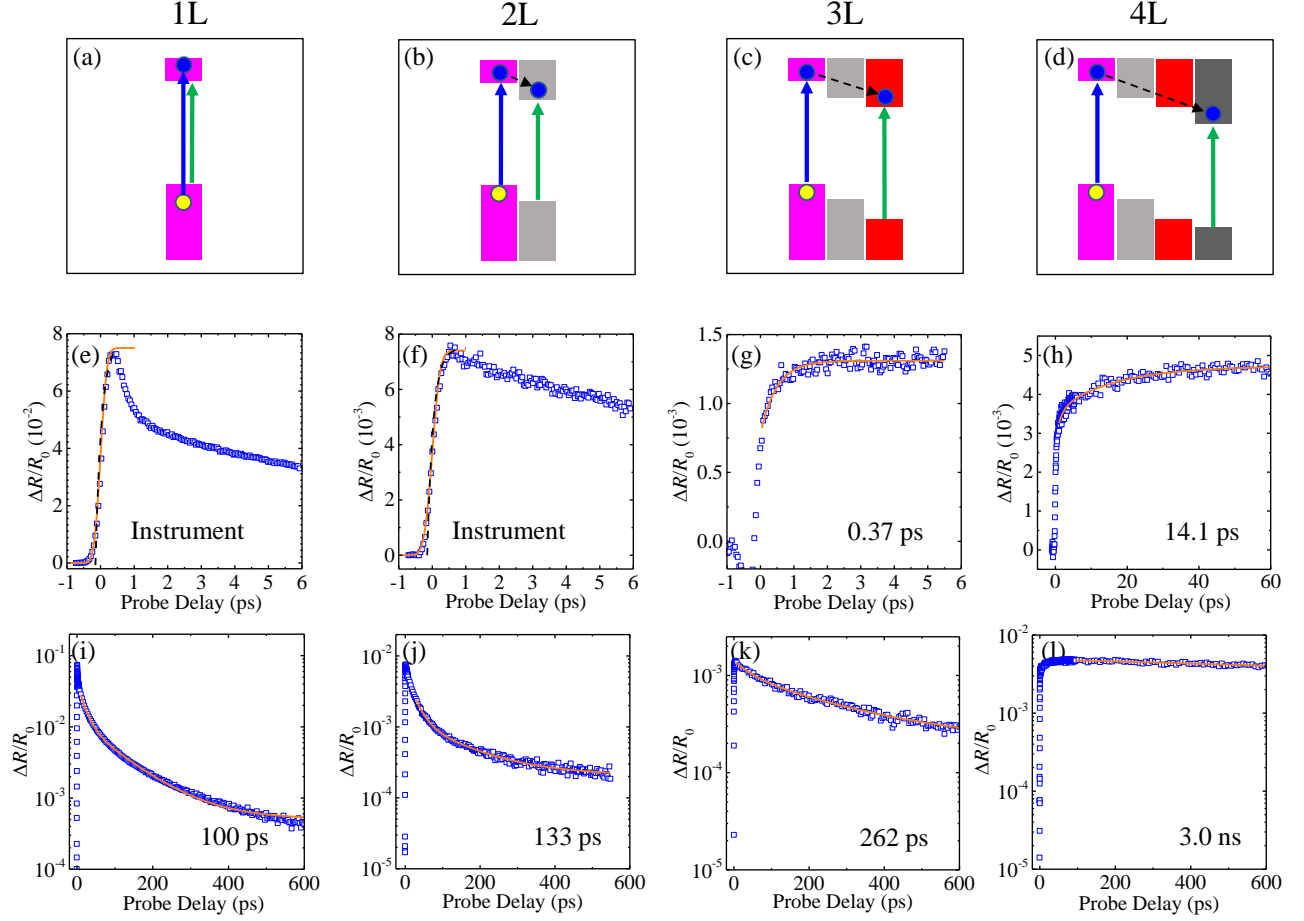


FIG. 3. Panels in the first row show the pump-probe configurations and expected electron transfer in the 4 samples. Blue and green arrows represent energies of the pump and probe photons. The observed differential reflection signals are plotted as blue symbols in the second and third rows, for short and long time ranges, respectively. The orange curves in (e) and (f) are integrals of a Gaussian function with a width of 0.35 ps, representing the cross-correlation of the pump and probe pulses. The dashed curves in (e) and (f) are exponential fits to the response functions, showing the time resolution of 0.18 ps in terms of exponentially varying signals. The orange curves in (g) and (h) are exponential fits (with resulted time constants labeled in each panel).

function (with a constant baseline) with a time constant of 100 ps.

To measure the electron dynamics in the WSe₂-MoSe₂ 2L sample, we monitor the differential reflection of a probe pulse tuned near the A-exciton resonance of MoSe₂ (790 nm) after a 400-nm pump pulse non-resonantly injects photocarriers into both layers [Fig. 3(b)]. Given that the CBM is situated in the MoSe₂ layer, electrons in the conduction band of WSe₂ are predisposed to transfer

to MoSe₂, denoted by the black dashed arrow in (b). Similarly, holes in the valence band of MoSe₂ are inclined to transfer into WSe₂. Once electrons and holes separate between the layers, they are expected to form spatially indirect excitons, also known as interlayer or charge-transfer excitons. As a result of the spatial separation between the electron and the hole, their recombination will be suppressed and their lifetime will be extended. Figures 3(f) and (j) show the differential reflection of the 790 nm probe in a short and long time scales (blue squares), respectively. The signal immediately reaches its maximum value, within the instrument response time, and starts to decay shortly after. The decay constant of 133 ps extracted from an exponential fit [orange curve in (j)] is slightly larger than in WSe₂ 1L. Previously, increase of photocarrier lifetime in TMD hetero-bilayers has been observed by several groups^{22,47,53,54,56}, and was attributed to the effect of the spatial separation of the electrons and holes in interlayer excitons. Our result is consistent with these studies.

Moving on to the 3L sample, a 750-nm pump pulse injects photocarriers into MoSe₂ and WSe₂. A 620-nm probe pulse is used to detect the presence of electrons in top WS₂ layer [Fig. 3(c)]. As a result of the lower energy of the pump photons, the WS₂ layer is not excited; hence, differential reflection signal of the 620-nm probe is induced by electrons that are excited in the other two layers and transferred to WS₂. As shown in (g), after photoexcitation by the pump pulse, the signal quickly rises within the first 0.5 ps. Shortly after, the signal slowly rises and reaches its maximum value. Since the pump excites both MoSe₂ and WSe₂ layers, we attribute the ultrafast rise of the signal to the transfer of electrons from MoSe₂ into WS₂ and the relatively slower process to the transfer of electrons from WSe₂ into WS₂. To model the second temporal region, we fit the data with $N(t) = N_0[1 - \exp(-t/\tau)]$, where N_0 is the peak density and τ is the transfer time. The extracted transfer time from the fit (shown as the orange curve) is 0.37 ± 0.02 ps. As shown in (k), a slow decay of the signal occurs after 5 ps that last a few hundred picoseconds. As it is expected, the lifetime of the electrons in the 3L sample is extended to 262 ps.

The 4L sample was measured with the same 750-nm pump pulse, but with a probe tuned to the A-exciton of MoS₂ layer (620 nm), to where the electrons are expected to transfer [Fig. 3(d)]. The pump injects photocarriers into the WSe₂ and MoSe₂ layers, leaving the WS₂ and MoS₂ layers unexcited. We observed a much slower rising process in (h), which reflects the slow transfer of electrons from the bottom WSe₂ to the top MoS₂ layer in this 4L structure. This assignment is supported by the decay of the exciton population in the WSe₂ 1L. As shown in (i), about 90% of the injected excitons in the WSe₂ 1L decays in 70 ps due to their recombination, which is

approximately the time it takes for the signal to reach its maximum. Moreover, the WSe₂ PL peaks of the 3L and 4L are 4 and 24 counts per second, respectively [see Fig. 2(o) and (p)]. The higher PL yield from the 4L sample indicates that a higher fraction of electrons recombines in the WSe₂ layer of the 4L sample as a consequence of a less efficient electron transfer, further supporting this interpretation. We fit this electron transfer process with the same model as the 3L, and extracted a transfer time of 14.9 ± 1.8 ps. The slow decay of the signal after 70 ps shown in Fig. 3(l) is attributed to the extremely long lifetime of electrons in MoS₂ due to their large separation from the holes, which reside in WSe₂. By an exponential fit, we extract an electron lifetime of about 3.0 ns. Compared to the lifetime of excitons in individual 1Ls, the electron lifetime in the 4L sample is extended several hundred times.

D. Hole Transfer and Lifetime

We also measured the dynamics of holes in these samples by using the pump-probe configurations illustrated in the first row of Fig. 4. Since holes are expected to transfer to WSe₂, where the VBM resides, a 749-nm probe is used for all the samples. A 620-nm pump is used, with certain values of fluence so that for each sample, the total injected photocarrier density is 1.5×10^{11} cm⁻². Due to the small band gap of WSe₂, quantitative study of hole transfer is complicated by the fact that a pump pulse tuned to, for example, the exciton resonance of MoS₂, will inevitably excite WSe₂, too. The photocarriers directly injected in WSe₂ dominate the signal at early times. Nevertheless, as shown in the second row of Fig. 4, a trend of slower rising of the signal with more layers is visible. From measurements over long time ranges, as shown as the last row, the hole lifetimes are 134 ps, 346 ps, and 2.3 ns in the 2L, 3L, and 4L samples, respectively. These values are reasonably consistent with the electron lifetimes obtained in the previous section.

In all the multilayer samples studied, the interlayer twist angles were undetermined. Nevertheless, the electron transfer and recombination times obtained from multiple samples are reasonably consistent, and show systematic layer-number dependence. These results suggest that the twist angle does not influence the electron transfer and recombination significantly. Indeed, a recent comprehensive study on MoS₂-WSe₂ heterostructures with controlled twist angles did not observe clear correlations between the electron transfer and recombination times and the twist angle⁵⁷. Such a weak dependence could be attributed to defect-assisted recombination⁵⁷, relaxation of momentum conservation due to the localized states^{57,58}, and layer mixing of certain electronic states⁵⁹.

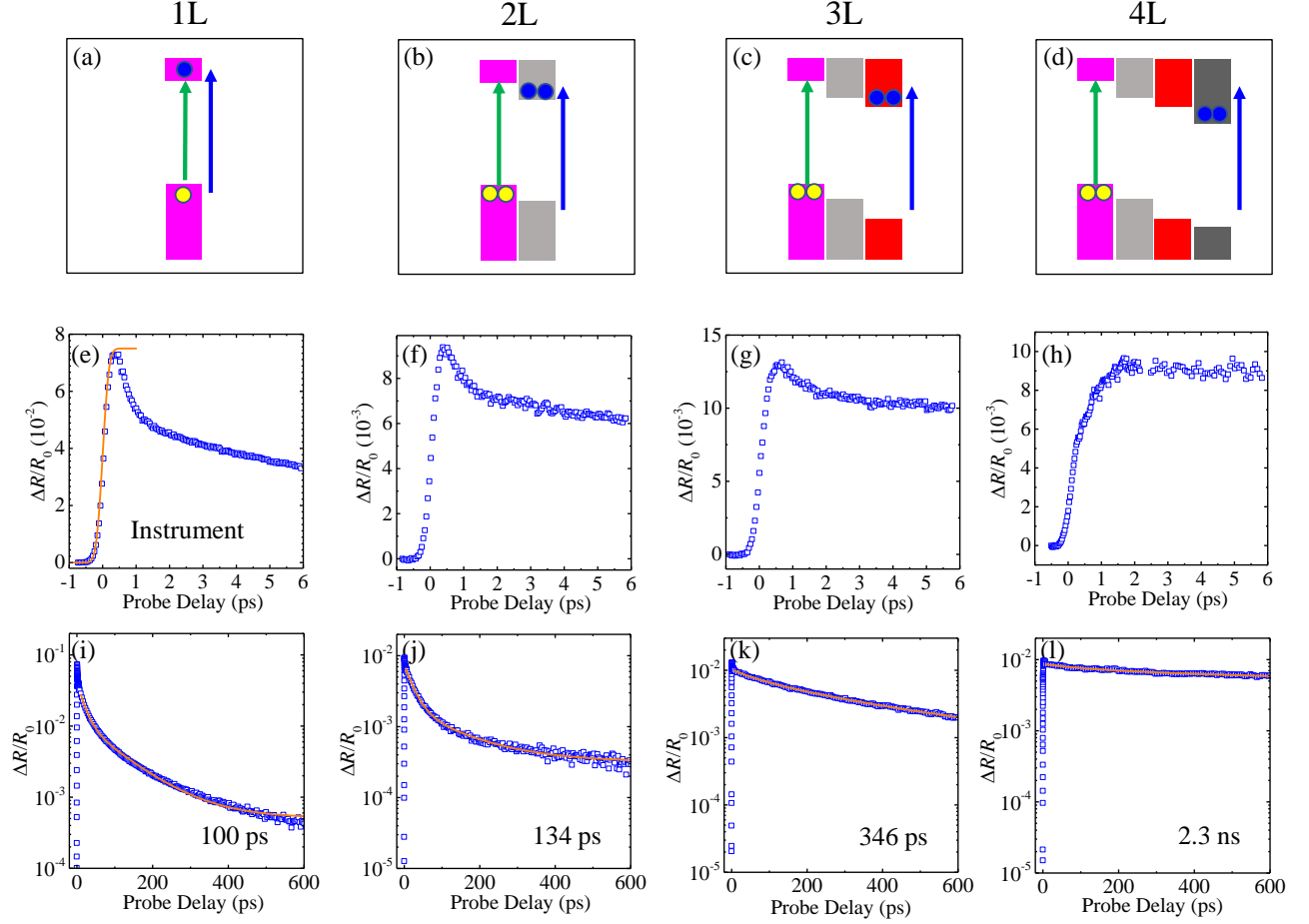


FIG. 4. Panels in the first row show the pump-probe configurations in the 4 samples. Blue and green arrows represent energies of the pump and probe photons. The observed differential reflection signals are plotted as blue symbols in the second and third rows, for short and long time ranges, respectively. The orange curves represent exponential fits (with resulted time constants labeled in each panel).

In future studies, it would be interesting to investigate the twist-angle dependence of electron dynamics in multilayer samples.

IV. CONCLUSION

By using four different TMD 1Ls, we have fabricated a set of samples of WSe_2 - MoSe_2 2L, WSe_2 - MoSe_2 - WS_2 3L, and WSe_2 - MoSe_2 - WS_2 - MoS_2 4L, and characterize their optical properties and photocarrier dynamics by conducting absorption, PL, and ultrafast pump-probe spectroscopy measurements. This set of multilayer samples were chosen with the intention of studying the be-

havior of electrons and holes as they are further separated from each other by 1L increments. The presented multilayer samples were atomically engineered to precisely achieve this purpose. We observed that the absorbance is higher in the multilayer structures when compared to the sum of the individual absorbances from the constituent 1Ls. Moreover, from the PL results we confirmed that we can effectively put up to 4 different 1Ls together with high quality interfaces that allow efficient interlayer charge transfer. We were also able to time-resolve the transfer of electrons between the layers and quantified how the lifetimes of the electrons and holes were extended as additional 1Ls were added. We show that the ultimate 4L sample with a thickness of 2.5 nm has an absorbance as high as 50% in the visible range. We found that the transfer time of electrons across the multilayer increases from a fraction of picosecond in 2L to about 14 ps in the 4L, while photocarrier lifetime is extended from about 100 ps to more than 3 ns in the 4L. The novel properties of these TMD multilayer heterostructures suggests promising potential applications in ultrathin, flexible, and efficient photovoltaic and photodetection devices. Furthermore, we demonstrated an approach for fabricating van der Waals multilayers that can be used to produce more complex multilayer structures with desired band alignment and optoelectronic properties for various applications.

V. ACKNOWLEDGEMENT

This material is based upon work supported by the National Science Foundation of USA under Award No. DMR-1505852.

* huizhao@ku.edu

¹ B. A. Bernevig and S. C. Zhang, *Phys. Rev. Lett.* **96**, 106802 (2006).

² M. König, S. Wiedmann, C. Brüne, A. Roth, H. Buhmann, L. W. Molenkamp, X. L. Qi, and S. C. Zhang, *Science* **318**, 766 (2007).

³ J. Kasprzak, M. Richard, S. Kundermann, A. Baas, P. Jembrun, J. M. J. Keeling, F. M. Marchetti, M. H. Szymanska, R. Andre, J. L. Staehli, V. Savona, P. B. Littlewood, B. Deveaud, and L. S. Dang, *Nature* **443**, 409 (2006).

⁴ K. S. Novoselov, A. K. Geim, S. V. Morozov, D. Jiang, Y. Zhang, S. V. Dubonos, I. V. Grigorieva, and A. A. Firsov, *Science* **306**, 666 (2004).

- ⁵ E. Gibney, *Nature* **522**, 274 (2015).
- ⁶ Q. H. Wang, K. Kalantar-Zadeh, A. Kis, J. N. Coleman, and M. S. Strano, *Nat. Nanotechnol.* **7**, 699 (2012).
- ⁷ S. Z. Butler, S. M. Hollen, L. Cao, Y. Cui, J. A. Gupta, H. R. Gutiérrez, T. F. Heinz, S. S. Hong, J. Huang, A. F. Ismach, E. Johnston-Halperin, M. Kuno, V. V. Plashnitsa, R. D. Robinson, R. S. Ruoff, S. Salahuddin, J. Shan, L. Shi, M. G. Spencer, M. Terrones, W. Windl, and J. E. Goldberger, *ACS Nano* **7**, 2898 (2013).
- ⁸ L. Zhong, M. Amber, B. Natalie, S. Shruti, Z. Kehao, S. Yifan, L. Xufan, J. B. Nicholas, Y. Hongtao, K. F.-S. Susan, C. Alexey, Z. Hui, M. Stephen, M. L. Aaron, X. Kai, J. L. Brian, D. Marija, C. M. H. James, P. Jiwoong, C. Manish, E. S. Raymond, J. Ali, C. H. Mark, R. Joshua, and T. Mauricio, *2D Mater.* **3**, 042001 (2016).
- ⁹ Y. Zhang, Y. W. Tan, H. L. Stormer, and P. Kim, *Nature* **438**, 201 (2005).
- ¹⁰ K. S. Novoselov, A. K. Geim, S. V. Morozov, D. Jiang, M. I. Katsnelson, I. V. Grigorieva, S. V. Dubonos, and A. A. Firsov, *Nature* **438**, 197 (2005).
- ¹¹ Y. Zhang, T. T. Tang, C. Girit, Z. Hao, M. C. Martin, A. Zettl, M. F. Crommie, Y. R. Shen, and F. Wang, *Nature* **459**, 820 (2009).
- ¹² J. B. Oostinga, H. B. Heersche, X. Liu, A. F. Morpurgo, and L. M. K. Vandersypen, *Nat. Mater.* **7**, 151 (2008).
- ¹³ B. E. Feldman, J. Martin, and A. Yacoby, *Nat. Phys.* **5**, 889 (2009).
- ¹⁴ M. F. Craciun, S. Russo, M. Yamamoto, J. B. Oostinga, A. F. Morpurgo, and S. Thruha, *Nat. Nanotechnol.* **4**, 383 (2009).
- ¹⁵ A. H. C. Neto, F. Guinea, N. M. R. Peres, K. S. Novoselov, and A. K. Geim, *Rev. Mod. Phys.* **81**, 109 (2009).
- ¹⁶ K. F. Mak, C. Lee, J. Hone, J. Shan, and T. F. Heinz, *Phys. Rev. Lett.* **105**, 136805 (2010).
- ¹⁷ A. Splendiani, L. Sun, Y. Zhang, T. Li, J. Kim, C. Y. Chim, G. Galli, and F. Wang, *Nano Lett.* **10**, 1271 (2010).
- ¹⁸ A. K. Geim and I. V. Grigorieva, *Nature* **499**, 419 (2013).
- ¹⁹ Y. Liu, N. O. Weiss, X. Duan, H.-C. Cheng, Y. Huang, and X. Duan, *Nat. Rev. Mater.* **1**, 16042 (2016).
- ²⁰ W. J. Yu, Y. Liu, H. Zhou, A. Yin, Z. Li, Y. Huang, and X. Duan, *Nat. Nanotechnol.* **8**, 952 (2013).
- ²¹ K. Roy, M. Padmanabhan, S. Goswami, T. P. Sai, G. Ramalingam, S. Raghavan, and A. Ghosh, *Nat. Nanotechnol.* **8**, 826 (2013).

- ²² X. Hong, J. Kim, S. F. Shi, Y. Zhang, C. Jin, Y. Sun, S. Tongay, J. Wu, Y. Zhang, and F. Wang, *Nat. Nanotechnol.* **9**, 682 (2014).
- ²³ F. Withers, O. D. Pozo-Zamudio, A. Mishchenko, A. P. Rooney, A. Gholinia, K. Watanabe, T. Taniguchi, S. J. Haigh, A. K. Geim, A. I. Tartakovskii, and K. S. Novoselov, *Nat. Mater.* **14**, 301 (2015).
- ²⁴ H. Fang, C. Battaglia, C. Carraro, S. Nemsak, B. Ozdol, J. S. Kang, H. A. Bechtel, S. B. Desai, F. Kronast, A. A. Unal, G. Conti, C. Conlon, G. K. Palsson, M. C. Martin, A. M. Minor, C. S. Fadley, E. Yablonovitch, R. Maboudian, and A. Javey, *Proc. Natl. Acad. Sci. U. S. A.* **111**, 6198 (2014).
- ²⁵ P. Rivera, K. L. Seyler, H. Y. Yu, J. R. Schaibley, J. Q. Yan, D. G. Mandrus, W. Yao, and X. D. Xu, *Science* **351**, 688 (2016).
- ²⁶ O. B. Aslan, D. A. Chenet, A. M. van der Zande, J. C. Hone, and T. F. Heinz, *ACS Photon.* **3**, 96 (2016).
- ²⁷ H.-L. Liu, C.-C. Shen, S.-H. Su, C.-L. Hsu, M.-Y. Li, and L.-J. Li, *Appl. Phys. Lett.* **105**, 201905 (2014).
- ²⁸ Y. Li, A. Chernikov, X. Zhang, A. Rigosi, H. M. Hill, A. M. van der Zande, D. A. Chenet, E.-M. Shih, J. Hone, and T. F. Heinz, *Phys. Rev. B* **90**, 205422 (2014).
- ²⁹ H. Shi, R. Yan, S. Bertolazzi, J. Brivio, B. Gao, A. Kis, D. Jena, H. G. Xing, and L. Huang, *ACS Nano* **7**, 1072 (2012).
- ³⁰ Q. Wang, S. Ge, X. Li, J. Qiu, Y. Ji, J. Feng, and D. Sun, *ACS Nano* **7**, 11087 (2013).
- ³¹ H. N. Wang, C. J. Zhang, and F. Rana, *Nano Lett.* **15**, 339 (2015).
- ³² N. Kumar, Q. Cui, F. Ceballos, D. He, Y. Wang, and H. Zhao, *Phys. Rev. B* **89**, 125427 (2014).
- ³³ C. Mai, Y. G. Semenov, A. Barrette, Y. F. Yu, Z. H. Jin, L. Y. Cao, K. W. Kim, and K. Gundogdu, *Phys. Rev. B* **90**, 041414 (2014).
- ³⁴ J. He, D. He, Y. Wang, Q. Cui, F. Ceballos, and H. Zhao, *Nanoscale* **7**, 9526 (2015).
- ³⁵ Q. Cui, F. Ceballos, N. Kumar, and H. Zhao, *ACS Nano* **8**, 2970 (2014).
- ³⁶ T. Korn, S. Heydrich, M. Hirmer, J. Schmutzler, and C. Schueller, *Appl. Phys. Lett.* **99**, 102109 (2011).
- ³⁷ D. Lagarde, L. Bouet, X. Marie, C. R. Zhu, B. L. Liu, T. Amand, P. H. Tan, and B. Urbaszek, *Phys. Rev. Lett.* **112**, 047401 (2014).
- ³⁸ C. J. Docherty, P. Parkinson, H. J. Joyce, M. H. Chiu, C. H. Chen, M. Y. Lee, L. J. Li, L. M. Herz, and M. B. Johnston, *ACS Nano* **8**, 11147 (2014).
- ³⁹ G. Wang, E. Palleau, T. Amand, S. Tongay, X. Marie, and B. Urbaszek, *Appl. Phys. Lett.* **106**, 112101 (2015).
- ⁴⁰ L. Yuan and L. B. Huang, *Nanoscale* **7**, 7402 (2015).
- ⁴¹ T. Yan, X. Qiao, X. Liu, P. Tan, and X. Zhang, *Appl. Phys. Lett.* **105**, 101901 (2014).

- ⁴² F. Ceballos and H. Zhao, *Adv. Funct. Mater.* **27**, 1604509 (2017).
- ⁴³ Y. Z. Guo and J. Robertson, *Appl. Phys. Lett.* **108**, 233104 (2016).
- ⁴⁴ C. Gong, H. J. Zhang, W. H. Wang, L. Colombo, R. M. Wallace, and K. J. Cho, *Appl. Phys. Lett.* **103**, 053513 (2013).
- ⁴⁵ F. Ceballos, M. Z. Bellus, H. Y. Chiu, and H. Zhao, *Nanoscale* **7**, 17523 (2015).
- ⁴⁶ A. F. Rigos, H. M. Hill, Y. L. Li, A. Chernikov, and T. F. Heinz, *Nano Lett.* **15**, 5033 (2015).
- ⁴⁷ F. Ceballos, M. Z. Bellus, H. Y. Chiu, and H. Zhao, *ACS Nano* **8**, 12717 (2014).
- ⁴⁸ A. Vašíček and H. Watney-Kaczér, “Optics of thin films,” (North-Holland Pub, Netherlands, 1960) pp. 179–181.
- ⁴⁹ P. Rivera, J. R. Schaibley, A. M. Jones, J. S. Ross, S. Wu, G. Aivazian, P. Klement, K. Seyler, G. Clark, N. J. Ghimire, J. Yan, D. G. Mandrus, W. Yao, and X. Xu, *Nat. Commun.* **6**, 6242 (2015).
- ⁵⁰ C. H. Lee, G. H. Lee, A. M. van der Zande, W. Chen, Y. Li, M. Han, X. Cui, G. Arefe, C. Nuckolls, T. F. Heinz, J. Guo, J. Hone, and P. Kim, *Nat. Nanotechnol.* **9**, 676 (2014).
- ⁵¹ M. M. Furchi, A. Pospischil, F. Libisch, J. Burgdorfer, and T. Mueller, *Nano Lett.* **14**, 4785 (2014).
- ⁵² S. Tongay, W. Fan, J. Kang, J. Park, U. Koldemir, J. Suh, D. S. Narang, K. Liu, J. Ji, J. Li, R. Sinclair, and J. Wu, *Nano Lett.* **14**, 3185 (2014).
- ⁵³ M. Z. Bellus, F. Ceballos, H.-Y. Chiu, and H. Zhao, *ACS Nano* **9**, 6459 (2015).
- ⁵⁴ K. Wang, B. Huang, M. Tian, F. Ceballos, M.-W. Lin, M. Mahjouri-Samani, A. Boulesbaa, A. A. Puretzy, C. M. Rouleau, M. Yoon, H. Zhao, K. Xiao, G. Duscher, and D. B. Geohegan, *ACS Nano* **10**, 6612 (2016).
- ⁵⁵ P. Nagler, G. Plechinger, M. V. Ballottin, A. Mitioglu, S. Meier, N. Paradiso, C. Strunk, A. Chernikov, P. C. M. Christianen, C. Schuller, and T. Korn, *2D Mater.* **4**, 025112 (2017).
- ⁵⁶ B. Peng, G. Yu, X. Liu, B. Liu, X. Liang, L. Bi, L. Deng, T. C. Sum, and K. P. Loh, *2D Mater.* **3**, 025020 (2016).
- ⁵⁷ H. M. Zhu, J. Wang, Z. Z. Gong, Y. D. Kim, J. Hone, and X. Y. Zhu, *Nano Lett.* **17**, 3591 (2017).
- ⁵⁸ X. Zhu, N. R. Monahan, Z. Gong, H. Zhu, K. W. Williams, and C. A. Nelson, *J. Am. Chem. Soc.* **137**, 8313 (2015).
- ⁵⁹ Y. Wang, Z. Wang, W. Yao, G. B. Liu, and H. Y. Yu, *Phys. Rev. B* **95**, 115429 (2017).